SPECIAL TOPIC • OPEN ACCESS

Access and sustainment of naturally ELM-free and small-ELM regimes

To cite this article: E. Viezzer 2018 *Nucl. Fusion* **58** 115002

OPEN ACCESS
IOP Publishing | International Atomic Energy Agency
Nuclear Fusion
Nucl. Fusion **58** (2018) 115002 (12pp)
https://doi.org/10.1088/1741-4326/aac222

Special Topic

Access and sustainment of naturally ELM-free and small-ELM regimes

E. Viezzer

Department of Atomic, Molecular and Nuclear Physics, University of Seville, Avda. Reina Mercedes, 41012 Seville, Spain

E-mail: eviezzer@us.es

Received 8 March 2018, revised 19 April 2018
Accepted for publication 3 May 2018
Published 27 September 2018

Abstract

Edge localized modes (ELMs) have a detrimental effect on the plasma facing components and pose one of the most serious obstacles for steady-state operation in a future fusion device. For future fusion machines, the control or even full suppression of ELMs is mandatory. In the past years, extensive effort has been directed to the development of operational regimes that maintain the high confinement and good performance of the H-mode, while at the same time ELMs are suppressed or mitigated. Several natural ELM-free and small-ELM regimes, such as the quiescent H-mode, the improved energy confinement mode, the type-II and the grassy ELM-regime, have been obtained in various tokamaks. The state-of-the-art and recent advances of these ELM-free and small-ELM scenarios are reviewed, and the access and sustainment as well as their applicability to ITER are discussed.

Keywords: magnetic confinement fusion, tokamaks, plasma transport, magnetohydrodynamics

(Some figures may appear in colour only in the online journal)

1. Introduction

Future fusion devices such as ITER [1] foresee the high-confinement mode (H-mode) [2] as the baseline operational scenario. The onset of the H-mode, achieved above a certain power threshold, is characterized by the formation of an edge transport barrier, a narrow region of reduced energy and particle transport. This transport barrier is responsible for steep edge temperature and density gradients, thus resulting in a steeper pressure profile at the edge compared to the low confinement mode (L-mode). A characteristic pedestal structure with high edge temperature and density is formed which determines the increase in particle and energy confinement found in the H-mode.

The sharp gradients of the H-mode edge region are limited by the occurrence of edge localized modes (ELMs) [3–7], magnetohydrodynamic (MHD) instabilities that expel particles and energy from the plasma and lead to a transient degradation of the transport barrier. There are different types of ELMs [3, 6, 7], the large and periodic type-I ELM being the most serious concern for future fusion devices. For type-I ELMs, this limit is believed to be defined by the peeling-ballooning limit [8–11], driven by an interplay between the edge pressure gradient ∇p and current density j. The energy exhaust during an ELM can account for up to 30% of the total stored energy in the plasma. For future magnetic fusion devices, the mitigation or even full suppression of ELMs is mandatory to avoid erosion of the divertor target plates from the heat and particle fluxes caused by a type-I ELM [12]. At the same time the pedestal top pressure should not be strongly reduced [13, 14] so as to maintain the good confinement of the H-mode.

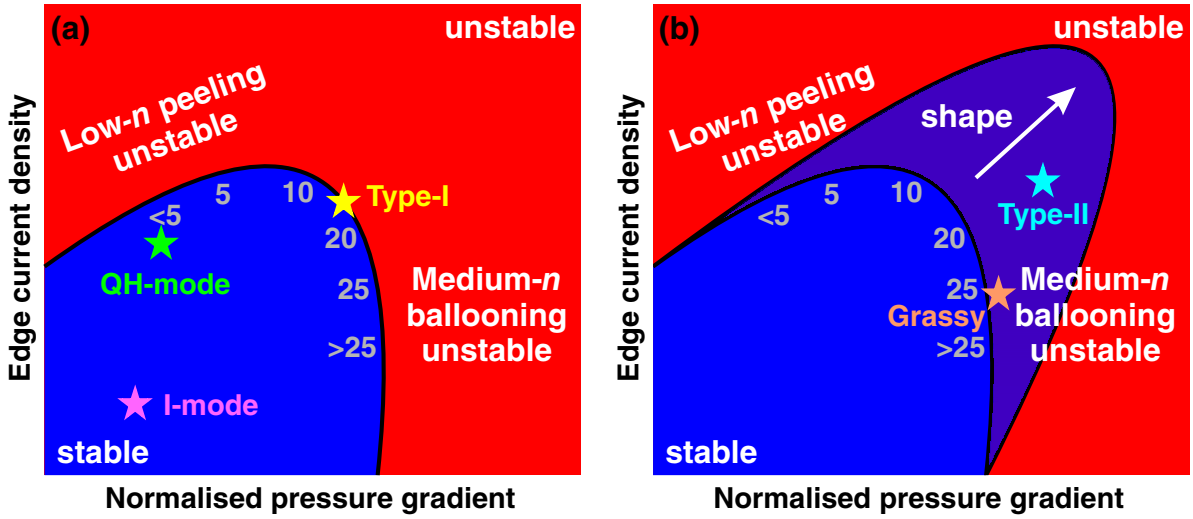

Figure 1. Schematic sketch of pedestal stability diagram: (*a*) shows typical experimental points of type-I ELMy regimes (yellow star), QH-modes (green star), I-modes (magenta star), (*b*) illustrates the experimental points of type-II ELMs (cyan star) and grassy ELMs (orange star).

In the pedestal region, three types of instabilities based on ideal MHD can occur. First, ballooning modes, with medium to high toroidal mode number (n), driven by the steep edge pressure gradient, which have their maximum amplitude on the outboard side. Second, low-n kink-peeling modes driven by the pedestal current and third, a combination of the two instabilities, i.e. coupled peeling-ballooning modes, driven by steep pressure gradients and large edge currents. Recent theoretical studies suggest that besides the global peeling-ballooning mode which affects the entire pedestal, local modes can exist that affect the plasma edge in a very narrow region [15, 16]. These local modes can drive transport, thus changing the pedestal structure locally [17, 18].

Figure 1 shows a schematic sketch of the pedestal stability diagram based on peeling-ballooning theory [10, 11], which depends on the maximum value of the normalised pedestal pressure gradient and the edge bootstrap current. When increasing the plasma shape the field line length in the bad curvature region is shorter [19], which helps to increase the stability boundary and thus, higher pressure gradients and edge currents can be reached before hitting the ELM stability limit. Modifying the transport and thus, changing the pedestal structure using actuators such as shaping or $\mathbf{E} \times \mathbf{B}$ rotation can affect the pedestal stability, thus opening a window for accessing a regime which features a pedestal that stays below the limit for type-I ELMs. Figures 1(*a*) and (*b*) show the operational points (coloured stars) of the quiescent H-mode (QH-mode), the improved energy confinement regime (I-mode), grassy ELMs and type-II ELMs discussed in this paper. The yellow star shows a typical operational point of a type-I ELMy H-mode plasma.

In the past years, extensive effort has been directed to the development of operational regimes that maintain the high confinement and performance of the H-mode, while at the same time eliminating and/or mitigating the ELMs (e.g. [20–27] and references therein). Here, we distinguish between *'natural' ELM-free regimes*, such as the QH-mode [20], the I-mode [21] and the enhanced D_α (EDA) H-mode at C-Mod [22], *small-ELM regimes*, such as grassy [28] and type-II ELMs [23], and *active ELM control techniques* [29, 30], such as externally applied magnetic perturbations [27, 31, 32], ELM pacing with pellets [33–35], vertical kicks [36, 37] or supersonic molecular beam injection (SMBI) [38, 39]. While pellet pacing and the application of externally applied magnetic perturbation coils are currently the foreseen path for ELM control in ITER, the underlying physics mechanisms and access conditions are not completely clear yet. Natural no-ELM and small-ELM regimes are potential candidates as they feature many aspects required for the operation of ITER and future fusion devices. In the past years, substantial progress on expanding the operational window of natural no-ELM and small-ELM regimes has been made such that they could possibly be used in ITER.

A review of the current understanding of natural ELM-free and small-ELM regimes is presented in this paper, summarizing the recent advances made in the last 2–3 years. For recent work in understanding the effects of active ELM control techniques, the reader is referred to [30].

This paper is organized as follows: section 2 discusses the advances made for the I-mode [21, 40] and QH-mode [20, 41–43], two regimes which occur naturally without ELMs. In section 3, the recent progress for type-II ELMs [44] and grassy ELMs [28] is presented. Section 4 discusses the projection of these regimes towards ITER. Section 5 summarizes the findings and discusses the direction for future work.

2. Naturally ELM-free regimes

Naturally occurring ELM-free regimes, such as the improved energy confinement mode (I-mode) [21, 40] and the QH-mode [20] represent an attractive solution for ITER and future fusion devices. However, extrapolation of these regimes is still uncertain as a detailed physics understanding is not yet available. Significant progress on the I-mode and the QH-mode has been

made recently towards developing a complete physics basis. An overview of the state-of-the-art is given in this section.

2.1. The improved energy confinement mode (I-mode)

The I-mode [21], originally dubbed improved L-mode on ASDEX Upgrade [40] due to the weaker power degradation compared to the L-mode [45], is characterized by an increased temperature gradient at the edge and higher energy confinement with respect to the L-mode. The particle transport remains close to the L-mode level. In this regime, the energy and particle transport are decoupled as the pedestal build-up is only observed in the temperature but not in the density. The energy confinement factor $H_{98}(y,2)$ in the I-mode usually ranges between 0.6–1.0 [46–48] and values up to 1.2 have been observed recently [49]. I-modes that can be sustained over several confinement times at AUG show confinement levels of $H_{98}(y,2) \leqslant 0.85$ [47]. On Alcator C-Mod stationary I-modes reached confinement factors of up to 1.0–1.2 [48]. The I-mode is typically accessed in the unfavourable ∇B drift configuration (unfavourable regarding H-mode access), where the ion ∇B drift is away from the active X-point, which exhibits a higher L-H power threshold compared to the favourable configuration. The onset of the I-mode is detected by the increase in the pedestal temperature, concomitant with an increase in the pressure and global energy confinement. In addition to the formation of a temperature pedestal, a weakly coherent mode (WCM, at frequencies of 100–300 kHz) [50], localized at the very edge of the plasma [51], and a geodesic acoustic mode (GAM, at frequencies of 10–30 kHz) are observed [52, 53]. The GAM has been shown to be responsible for the broadband structure of the WCM [52, 53], which thus represents a non-linearly coupled system.

Figure 2 shows example time traces from Alcator C-Mod [48]. The onset of the I-mode is highlighted by the dashed, vertical line. As shown, the density and the D_α emission stay close to L-mode levels, while the electron temperature is increased by a factor of 2, leading to the improved confinement. Access to the I-mode has been observed with different heating methods, including neutral beam injection, electron and ion cyclotron resonance heating [47, 48]. Further, the access is independent of the wall material, as the I-mode confinement regime was obtained on AUG with the carbon [40] and tungsten wall [47], and on Alcator C-Mod (Mo wall) [21, 48] and DIII-D (C wall) [48, 54]. The main features of the I-mode (temperature pedestal, ELM-free, increased stored energy) were observed to be universal in all three devices.

Recently, an I-mode database was compiled on AUG including I-modes in the upper-single null (USN) configuration and in reversed B_t/I_p in the lower single null (LSN) configuration (both with the ion ∇B drift away from the active X-point), covering magnetic fields of 1.8–3.0 T [46]. The auxiliary heating power needed to induce the L-I transition depends on the line-averaged density, in line with observations on Alcator C-Mod [55]. The fact that no difference is seen between USN and LSN (with reversed B_t/I_p) indicates that the I-mode physics is independent of how the high power

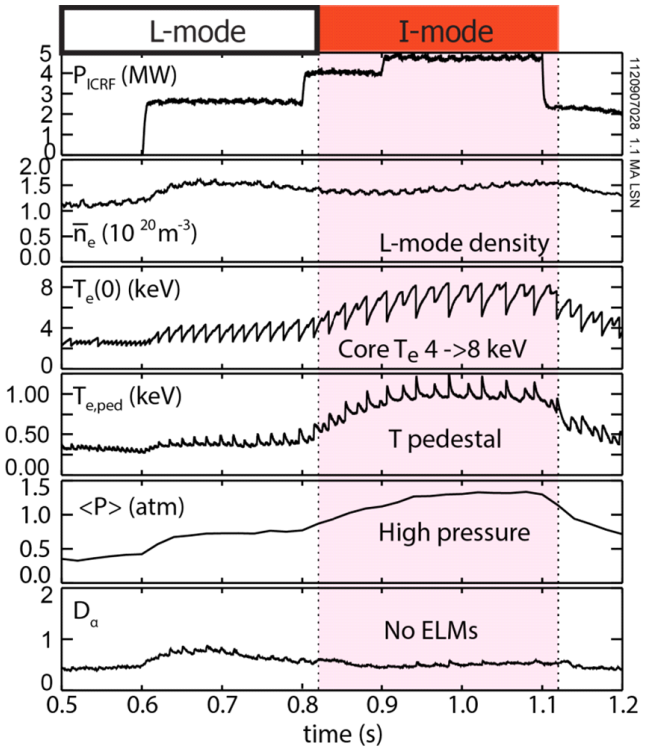

Figure 2. Transition from L- to I-mode on Alcator C-Mod: (*a*) ion cyclotron resonance frequency (ICRF) power, (*b*) line-integrated electron density, (*c*) core electron temperature, (*d*) pedestal electron temperature, (*e*) plasma pressure, (*f*) D_α emission used as ELM monitor. Reproduced courtesy of IAEA. Figure from [48]. © 2016 EURATOM.

threshold is obtained (either by reversing the field in LSN or operating with a forward field in USN) [47] as long as the ion ∇B drift is away from the X-point. The density dependence of the L-I power threshold has been studied and a different value in the power threshold is observed at low density when heating the electrons exclusively with ECRH (see figure 3). In this case, the L-I power threshold is increased by a factor of 2–3 [47]. Analysis of the edge ion heat flux at the L-I transition shows a linear dependence on the density and describes the behaviour also at low density (see figure 3). This is similar to results observed for the L-H transition [56]: a minimum edge ion heat flux is required in order to enter the I-mode. At low density, where ions and electrons are weakly coupled, more ECRH power is required in order to reach the necessary ion heat flux to enter the I-mode. As the edge E_r is mainly driven by the main ion pressure gradient [57–60], this also indicates that the E_r well could play a key role for the L-I transition. Compared to the scaling found for the L-H transition [61], the L-I transition shows a weak dependence on the magnetic field [46], in line with observations at Alcator C-Mod covering a range of 2.8–8 T [49]. Thus, the $\mathbf{E} \times \mathbf{B}$ shear stabilization may only play a minor role for triggering the I-mode. The edge radial electric field is observed to deepen at the L-I transition [46, 62]. Detailed measurements with Doppler reflectometry showed that at the onset of the I-mode in NBI-heated plasmas, first the inner E_r shear layer steepens, followed by a deepening of the E_r well during the I-mode as the temperature pedestal

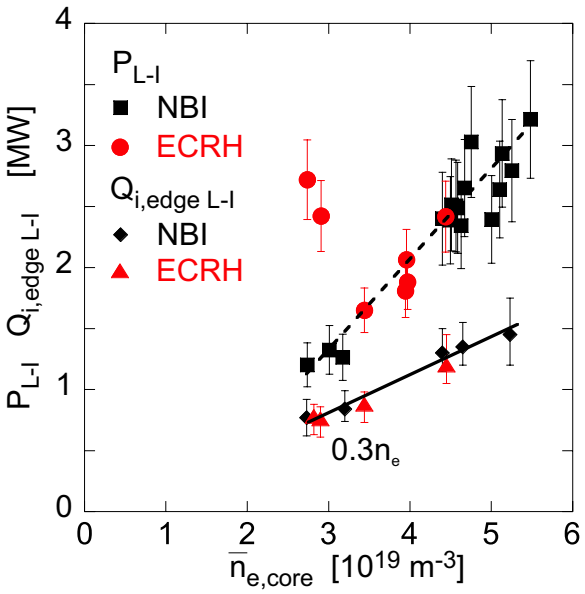

Figure 3. L-I power threshold and edge ion heat flux, $Q_{i,edge}$ at the L-I transition as a function of density at AUG. Reproduced courtesy of IAEA. Figure from [47]. © 2017 EURATOM.

evolves [46]. At the transition from I- to H-mode, the E_r well reaches values of around $-14\,\mathrm{kV\,m^{-1}}$, which is similar to the value observed at the L-H transition in the favourable configuration [63, 64].

Recent experiments on AUG also revealed the existence of strongly intermittent density fluctuations during the I-mode [65] which corresponds to the 'macroscopic fluctuations' mentioned in [40]. Figure 4 shows the behaviour of the fluctuation amplitude measured with Doppler reflectometry at the plasma edge of the (*a*) L-mode and (*b*) I-mode. Compared to the L-mode, the I-mode exhibits a lower baseline level but shows strongly intermittent events with a much larger fluctuation amplitude [65]. These bursts typically last for 2–10 μs and only appear during the I-mode. Figure 4(*c*) shows the evolution of the probability density function of the turbulence amplitude from L-, to I-, to H-mode. Note that here the fluctuation amplitude is normalized to the standard deviation in L-mode. While the low fluctuation amplitudes decrease from L- to I-mode, the large fluctuation amplitudes increase and the probability density function broadens. This behaviour was observed at all measured structure sizes, scanning the perpendicular wavenumber from 5–12 $\mathrm{cm^{-1}}$ [46].

The density fluctuations are correlated with the WCM [65]. The Doppler peak in the frequency spectrum appears quantized and shows multiple narrow sub-peaks (see figure 4(*d*)). Detailed analysis of these sub-peaks shows that the signal is amplitude modulated (non-sinusoidal) with the WCM frequency [65]. The large intermittent events are preceded by smaller density perturbations, which also show a correlation with the WCM frequency as the temporal difference between the preceding bursts is proportional to the inverse WCM frequency. These bursts have been observed in reflectometry, Doppler reflectometry, magnetic probes and bolometry and may play a decisive role in inhibiting the formation of a particle transport barrier in the I-mode [46]. Comparison of the

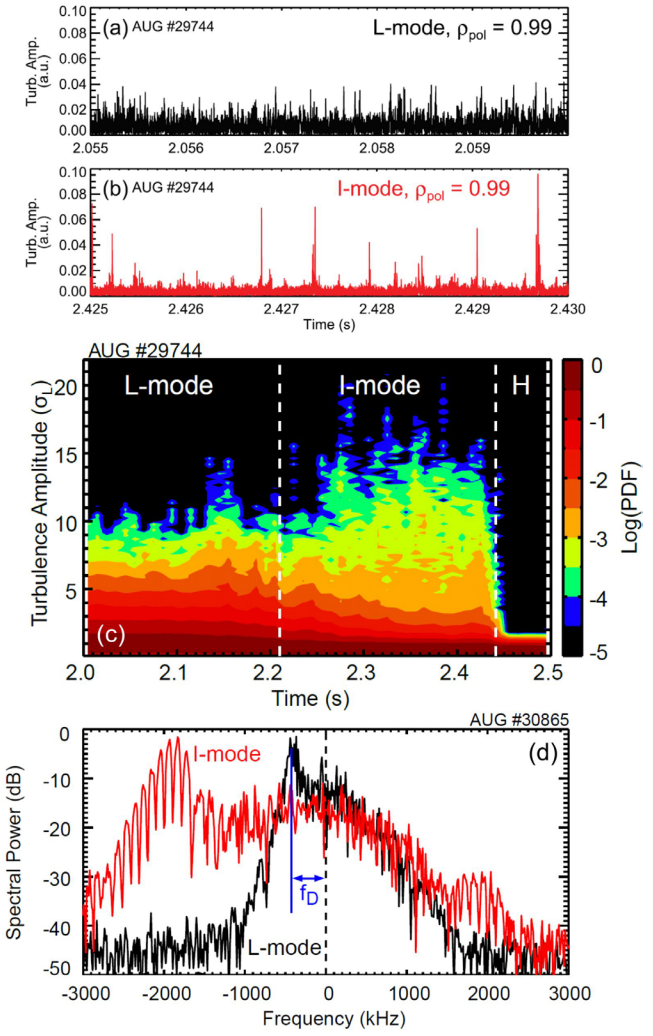

Figure 4. Fluctuation amplitudes measured at AUG in (*a*) L-mode and (*b*) I-mode. (*c*) Shows the probability density function during the transition from L- to I- to H-mode. (*d*) Shows the frequency spectra measured in L-mode (black) and I-mode (red). (*a*, *b*) Reproduced courtesy of IAEA. Figure from [66]. © 2017 EURATOM. (c, d) Reproduced courtesy of IAEA. Figure from [65]. © 2016 EURATOM.

Doppler reflectometry measurements, which are taken inside the confined region, to the bolometry signal in the divertor show a strong correlation with the fluctuation amplitude. The observed time delay between the two diagnostics indicates that the intermittent density bursts are born inside the separatrix and then travel towards the divertor [46]. The exact generation mechanism of these bursts is not clear yet. A non-linear electrostatic drift wave model has been proposed in [65], similar to the Korteweg–de-Vries and Burgers equation for intermittency in 1D systems.

The ELM-free I-mode regime with H-mode like energy transport, but L-mode like particle transport is favourable for future fusion devices as it avoids impurity accumulation and provides steady density profiles. The I-mode has been observed over a wide range in collisionality and q_{95} [21, 46–48], in particular at ITER-relevant values (see also section 4). Future studies should assess whether a sufficient amount of fusion power can be obtained without a density pedestal. In addition, future work should also focus on the transition

from I- to H-mode as it is still poorly understood and sets the operational limit for the I-mode. The fact that the I-mode has so far only been obtained robustly in the unfavourable configuration also means a higher power threshold compared to the usual L-H power threshold in the favourable configuration. Detailed studies on the compatibility of this requirement for ITER and future fusion devices are indispensable. At AUG, the I-mode often evolves into the H-mode in an uncontrolled manner [47], thus, making the I-mode non-steady. This could be a serious issue for ITER and future fusion devices. Non-steady I-modes are also observed on C-Mod for lower fields (∼2.8 T), but most discharges at high field (>5 T) have stationary conditions [49]. Experiments on AUG are ongoing that focus on avoiding the evolution into H-mode by controlling the plasma energy using a feedback controlled heating power [67].

Dedicated experiments for the development of the I-mode regime on TCV were carried out recently, however, to date the I-mode has not been found yet at TCV [68]. At low magnetic field (the nominal field of TCV is 1.45 T) the multi-machine scaling [49] suggests a very narrow window in auxiliary power for the I-mode. Further experiments are scheduled for 2018.

2.2. The quiescent H-mode (QH-mode)

The QH-mode is a naturally ELM-free state which shows the good confinement of the H-mode but without the degradation of the pedestal by ELMs. The QH-mode was originally discovered at DIII-D [20] and later also observed on ASDEX Upgrade with a carbon (C) wall [41], JET-C [42, 69] and JT-60U [43]. The QH-mode is a steady, ELM-free regime with constant density and radiated power which can be sustained for several seconds (i.e. 25–30 energy confinement times) [70]. The onset of the QH-mode is accompanied by an Edge Harmonic Oscillation (EHO) which increases the edge particle transport to allow natural stability against an ELM [20]. Figure 5 shows time traces of a QH-mode discharge at DIII-D: (*a*) the plasma current and divertor D_α light, (*b*) the onset of an $n = 1$ EHO, (*c*) the energy confinement factor, (*d*) the line-averaged and pedestal electron density, (*e*) the NBI power and total radiated power and (*f*) the neutral beam torque. Here, negative values correspond to the counter-current direction. Figure 5(*g*) shows a spectrogram of an EHO. The EHO typically exhibits low toroidal mode numbers and multiple harmonics. Experiments on DIII-D showed that the EHO provides continuous particle transport such that the plasma stays below the ELM stability boundary [72].

At AUG with a carbon wall, the onset of the QH-mode was accompanied by two types of MHD modes which were localized at the plasma edge [41]. A low frequency (∼10 kHz) $n = 1$ EHO with harmonics up to $n = 11$ and a high-frequency oscillation (HFO), observed at 350 and 490 kHz (see figure 6), which is detected by a set of fast pick-up coils (sampling rate 2.5 MHz) that measure the radial magnetic field. They were both observed to rotate in the electron diamagnetic direction. The HFO exhibited bursts which are phase-correlated with the EHO [41]. The EHO showed characteristic fast drops in the radial magnetic field signal, which always occured at the end of an HFO burst (see figure 6). The HFO bursts were also

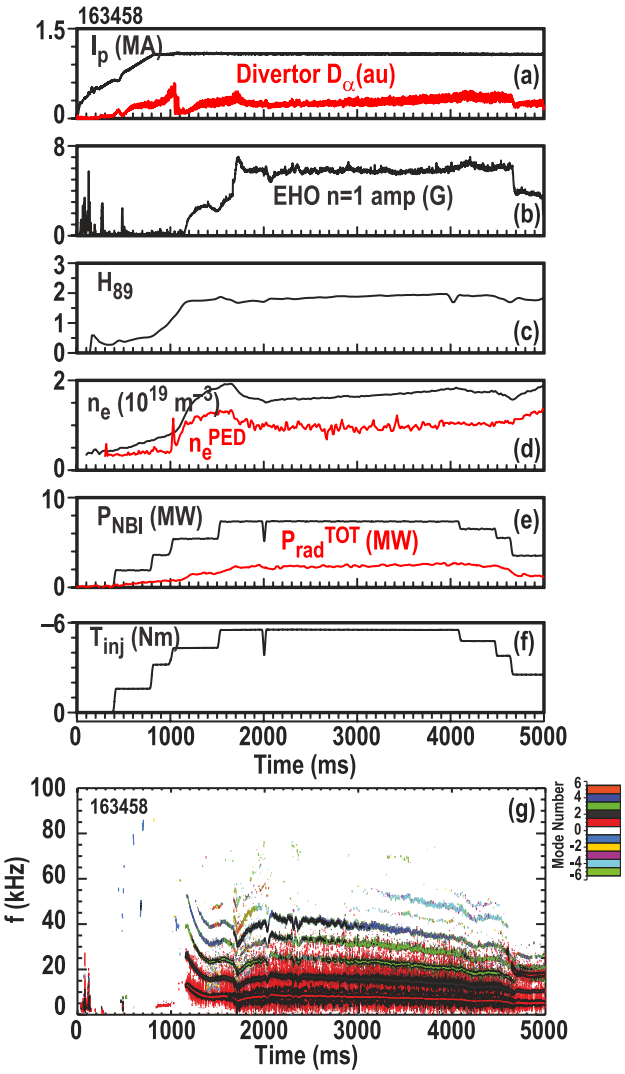

Figure 5. Time traces and magnetics spectrogram of a QH-mode plasma at DIII-D: (*a*) plasma current and divertor D_α light, (*b*) $n = 1$ component of coherent EHO, (*c*) energy confinement factor, (*d*) line-averaged and pedestal electron density, (*e*) NBI power and total radiated power, (*f*) neutral beam torque in counter-current direction. (*g*) Example magnetics spectrogram showing the edge harmonic oscillation. Reproduced from [71], with the permission of AIP Publishing.

visible in soft x-ray and in the D_α signal of the outer divertor [41].

At JET long-lived 'outer' modes were observed [42] and showed very similar characteristics as the EHO of the QH-mode. The outer mode has been identified as a current ribbon which controls transport across the pedestal. The current ribbon is located at a rational surface near the pedestal flat-top, and spins toroidally with the local plasma toroidal rotation frequency [42]. The mode appears at low to medium density, and was shown to significantly delay the first ELM. The existence of the current ribbon appears to depend on sufficient edge rotational shear [42].

The EHO is thought to be a saturated kink-peeling mode, driven unstable by large edge current densities. Recent nonlinear simulations with the 3D MHD code JOREK [73] and NIMROD [74] confirm this hypothesis [75–78]. For the

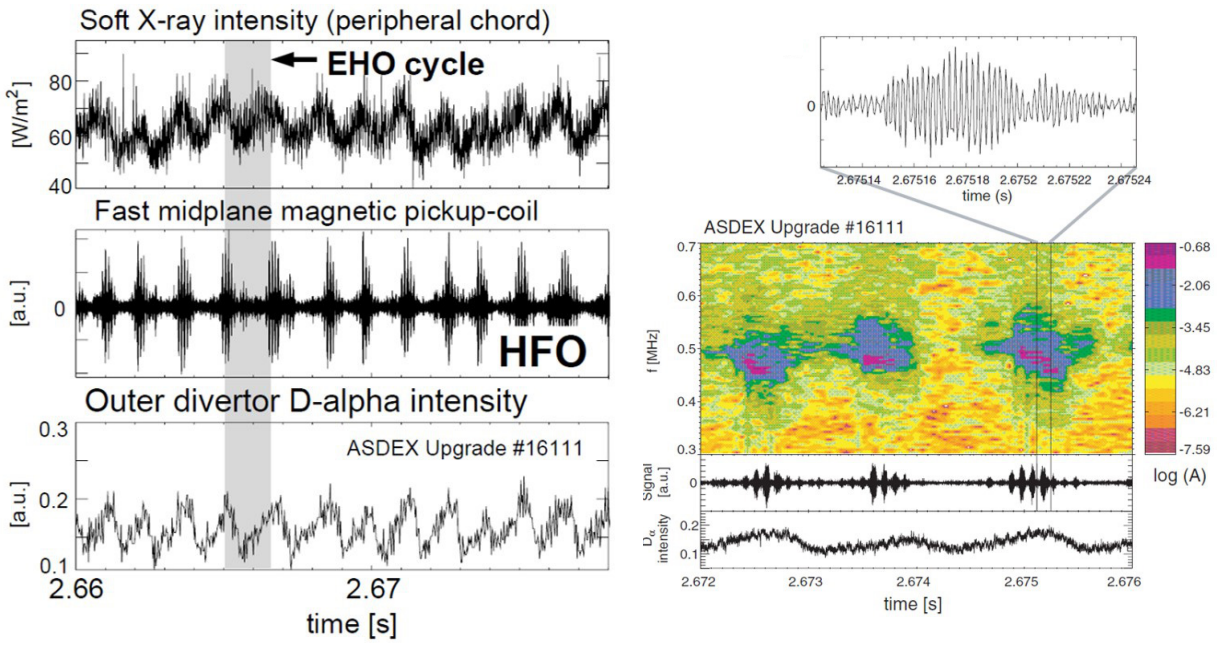

Figure 6. QH-mode at AUG-C: The left panel shows time traces of the soft x-ray intensity, a fast magnetic pick-up coil in the midplane, and the D_α intensity of the outer divertor. The right panel shows the spectrogram obtained from the fast pick-up coils, showing the HFO at ∼0.5 MHz. The HFO is correlated to the EHO and to changes in the D_α signal indicating particle transport. Reproduced from [41].

JOREK simulations, toroidal mode numbers up to $n = 10$ were included and reproduced the kink/peeling mode structure [75, 76]. The simulations show two phases: first, an initial linear growth phase which is dominated by high-n mode numbers, exhibiting the behaviour of an ELM-like burst. This is followed by a saturated phase, during which low-n kink/peeling modes grow to a saturated level and reach a 3D quasi-stationary state. Due to non-linear mode coupling [79] between the higher-n mode numbers, the $n = 1$ and 2 harmonics are excited later in time and then evolve to being the predominant perturbations in the stationary state. The simulations also reveal that the density perturbation has a 3D helical structure at the separatrix [75]. The kink-peeling mode causes an oscillation of the plasma boundary of 1.5 cm at the outer midplane. The simulated level of particle losses, the density fluctuations and the frequency spectrum are in agreement with the experiment [75]. A scan in pedestal pressure and edge current density was performed in JOREK to study the response of the perturbations [76, 80]. Increasing the pedestal pressure or decreasing the edge current results in a similar behaviour compared to the reference experimental equilibrium [80]. An ELM-like behaviour was observed in the linear phase, followed by a stationary state with low-n modes being dominant. When the pedestal pressure was increased and the edge current density was decreased simultaneously, the initial ELM-like linear phase was followed by a stationary state with a dominant ballooning mode with $n = 9, 10$. This indicates that a sufficiently high edge current density is needed to drive the EHO [76].

The operational window of the QH-mode was recently extended towards high Greenwald fraction [81] and low torque input [82]. Earlier experiments at DIII-D highlighted the key role of the $\mathbf{E} \times \mathbf{B}$ rotational shear for maintaining the QH-mode [83, 84]. This is supported by recent modelling with the M3D-C1 code [85]. Dedicated double torque ramp experiments show that the EHO appears above a critical $\mathbf{E} \times \mathbf{B}$ threshold and is replaced by ELMs below this threshold [86, 87]. The impact of the $\mathbf{E} \times \mathbf{B}$ rotation was also studied by means of non-linear modelling with JOREK [80]. First simulations scanning the $\mathbf{E} \times \mathbf{B}$ rotation profile up to 60% of the experimental profile show that the $n = 2$ mode already becomes dominant in the linear phase when including the $\mathbf{E} \times \mathbf{B}$ shear [80] (see figure 7). The $n = 2$ stays dominant in the saturated phase of the perturbed magnetic energy. These results are consistent with previous ideal MHD calculations, which showed that the shear in the toroidal rotation profile has a stabilizing effect for high-n modes [88].

The importance of the $\mathbf{E} \times \mathbf{B}$ rotational shear was also identified in nonlinear NIMROD simulations including toroidal mode numbers up to $n = 23$ [77, 78]. In this case a QH-mode with broadband MHD was simulated. The simulations suggest that rotational shear plays a critical role for the saturation mechanism. The stationary state is only achieved when including the $\mathbf{E} \times \mathbf{B}$ rotation. Without the $\mathbf{E} \times \mathbf{B}$ rotational shear the simulations exhibit an ELM-like behaviour [78]. This result differs somewhat from the JOREK simulations, as in those the saturated phase is also achieved without the $\mathbf{E} \times \mathbf{B}$ rotation. Further simulations including diamagnetic effects, neoclassical flows and a resistive wall are required to improve the predictive capability of non-linear MHD simulations.

Recently, a new wide-pedestal QH-mode regime was discovered in plasmas with double-null shape [71, 89]. In this

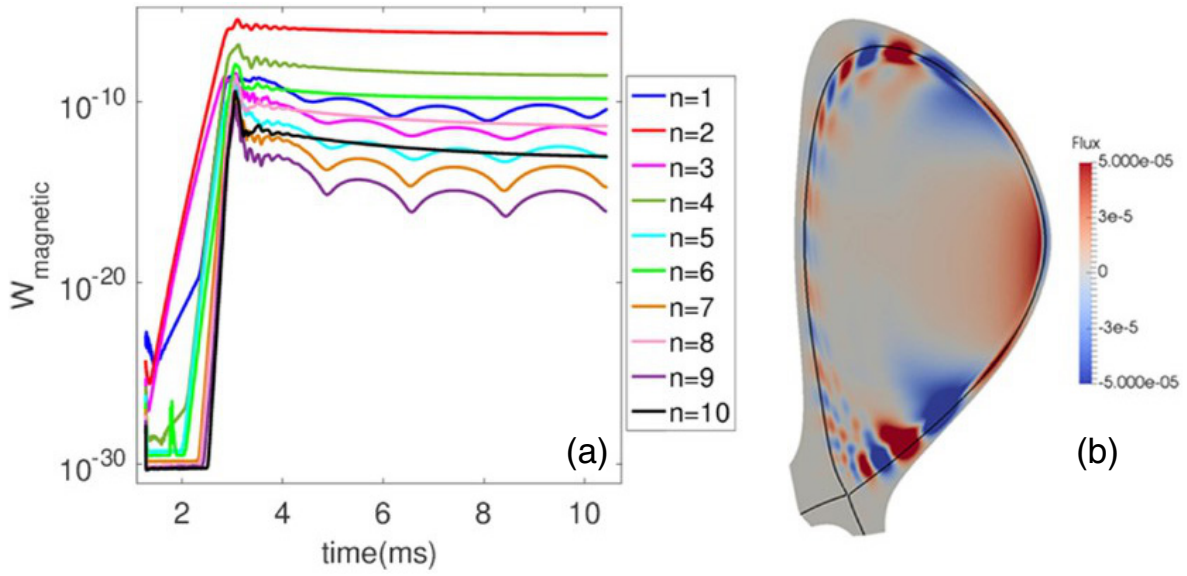

Figure 7. Nonlinear MHD simulations of a DIII-D QH-mode including an edge $\mathbf{E} \times \mathbf{B}$ rotation of 24 km s^{-1}: (*a*) time evolution of the perturbed magnetic energy of $n = 1 - 10$ modes, (*b*) contour plot showing the flux of the perturbation of $n = 1-10$ modes in a poloidal plane (with the separatrix in black) during the saturated phase. Reproduced from [80]. © IOP Publishing Ltd. All rights reserved.

shape, when reducing the net applied torque in a standard QH-mode, the plasma transits from a QH-mode with an EHO to this new regime characterized by broadband MHD and a wide pedestal. At the onset of this new regime, the pedestal width increases by 50%, the pedestal pressure increases by 60% and the global energy confinement by 40% (see figure 8) [71, 89]. The wide-pedestal QH-mode could be sustained over several seconds, as shown in figure 8. It was recently also obtained in shapes with upper and lower single null [90, 91]. Comparing the plasma profiles in the wide-pedestal QH-mode to a standard QH-mode shows that the steep gradient region moves inward and in the region where the standard QH-mode exhibits the steepest gradients, the profiles are now gentler. This is consistent with the observation that the $\mathbf{E} \times \mathbf{B}$ shear decreases at the very edge, but increases further inwards. This again highlights the importance of the $\mathbf{E} \times \mathbf{B}$ shear as this regime is only observed once the torque and therefore, the $\mathbf{E} \times \mathbf{B}$ shear, is reduced. Here, the following picture arises: As the torque is reduced, the $\mathbf{E} \times \mathbf{B}$ shear decreases giving rise to an increase of the edge MHD activity. This on the other hand can drive transport and thus, the gradients are reduced. The increased transport shifts the gradients in, allowing a broader pedestal. Combined with the high shaping, which affects the pedestal stability and pushes the boundary towards higher pressure gradients and edge currents, this leads to a broader and higher pedestal and the maximum gradient region is shifted further inwards compared to the standard QH-mode [71, 89].

This regime features improved confinement at low collisionality and low rotation, similar to the standard QH-mode at the same conditions [84], and could be a potential candidate for achieving high performance ELM-free operation at low torque. Further experiments are required to get a detailed understanding of the physics mechanism underlying the transition from the standard to the wide-pedestal QH-mode. To date, the wide-pedestal QH-mode has been accessed starting from a standard QH-mode. Experiments at DIII-D are ongoing to study whether this regime can be accessed directly.

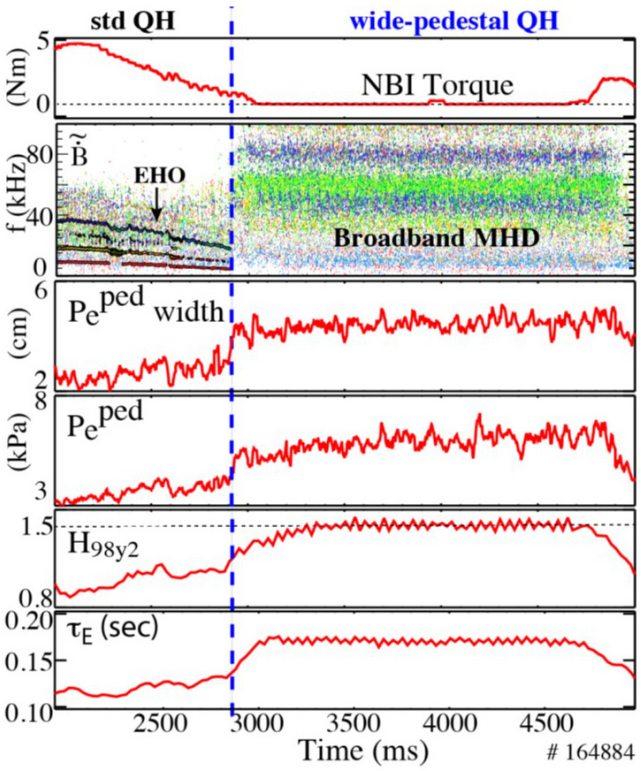

Figure 8. Transition from standard to wide-pedestal QH-mode at DIII-D: NBI torque, frequency spectogram, pedestal width of the electron pressure p_e, pedestal electron pressure, confinement factor $H_{98}(y,2)$ and energy confinement time. Reproduced courtesy of IAEA. Figure from [86]. Copyright 2017 IAEA.

3. Small ELM regimes

Several small ELM regimes were observed in AUG [23, 44], DIII-D [92], JET [93–95], JFT-2M [96], JT-60U [28], NSTX [97] and EAST [98]. An existence diagram is shown in figure 9, in which the ELM energy loss normalized to the pedestal stored energy, $\Delta W_{\mathrm{ELM}}/W_{\mathrm{ped}}$, is plotted against the normalized electron collisionality [99]. This diagram classifies the different types of ELMs [3] into the type-I ELMy regime, the type-III ELM regime and into small-ELM and no-ELM regimes (I-mode, QH-mode, EDA H-mode). The small-ELM regimes are characterized by reduced ELM energy losses with typically high ELM frequency. As shown in figure 9, different types of small ELMs were observed in different collisionality regimes. They all have in common that the observed ELM energy losses are smaller than 2 %. The type-V ELMy regime at NSTX [97], the high-recycling steady (HRS) H-mode on JFT-2M [96] and the type-II ELMs, observed on AUG [23, 44], DIII-D [92] and JET [93], have been observed at high collisionality values $\nu^*_{e,\mathrm{ped}} > 1-2$ [24]. A similar small ELM regime was obtained in strongly fuelled, high density plasmas with magnetic perturbations [100–102]. The grassy ELMs observed on JT60-U are typically accessed at low collisionalities $\nu^*_{e,\mathrm{ped}} < 0.2$.

In this paper, the focus is put on the grassy and type-II ELMs as they can be accessed 'naturally' by increasing the plasma triangularity. Both have in common that they are irregular, low-amplitude ELMs with high frequency and are observed when the plasma is put in-between the first and second stable ballooning regimes in the $s-\alpha$ diagram, where s is the normalized magnetic shear and α the normalized pressure gradient [92, 103, 104].

3.1. Type-II ELMs

A transition from type-I to type-II ELMs is observed when increasing the plasma density, edge safety factor and triangularity, moving the plasma close to a double-null configuration [23, 44]. Compared to type-I ELMs, the power load on the divertor of type-II ELMs reduces by a factor of 10 and the ELM affected area narrows down substantially [44].

Figure 10 shows the time evolution of the divertor current and the frequency spectrogram of the magnetics (a) and an ECE channel (b) at the plasma edge ($\rho_{\mathrm{pol}} = 0.9$). The onset of type-II ELMs is accompanied by a broadband fluctuation in the range of 30–50 kHz. The broadband oscillation is observed in the magnetics, microwave reflectometry and electron cyclotron emission diagnostic [23, 44]. The fluctuation is localized radially in the 'no-mans' land region up to the pedestal top ($0.75 < \rho_{\mathrm{pol}} < 0.95$). In this region, the T_e profile is slightly reduced, while n_e is unchanged (see figures 10(c) and (d)). Note that an increase in the scrape-off layer is observed [44, 105], suggesting that the scrape-off layer could play an important role for the type-II ELMs. Analysis of the temporal and spatial evolution of filaments of small ELMs on MAST and type-II ELMs on AUG [106] indicates that the toroidal mode number of these ELMs is a factor of 2 higher compared to

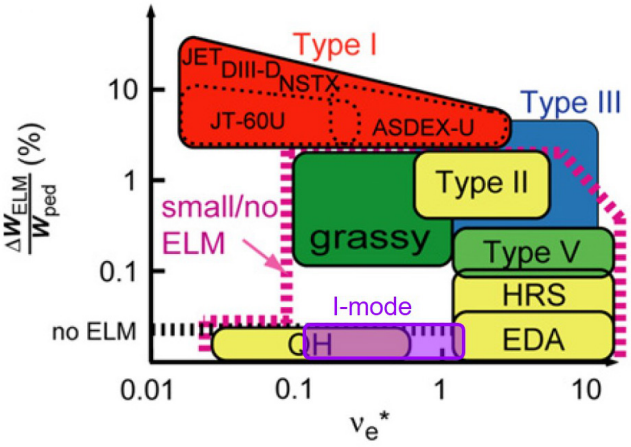

Figure 9. Normalized ELM energy loss, $\Delta W_{\mathrm{ELM}}/W_{\mathrm{ped}}$ versus pedestal electron collisionality for various small-ELM and no-ELM regimes. The type-I and type-III ELMy regimes are shown in red and blue. Reproduced from [99].

type-I ELMs. The importance of the scrape-off layer has also been highlighted in [106]. Here, the toroidal filament velocity is smaller compared to observations for type-I ELMs, suggesting that the filaments originate from the bottom of the pedestal.

The plasma shape, in this case the closeness to the double-null configuration, is one of the key parameters for obtaining type-II ELMs and indicates that the edge magnetic shear could play an important role [23, 105]. The closeness to the double-null shape expands the stable region [104]. In addition, at high density and low temperature, i.e. high collisionality, the stability boundary is set by high-n ballooning modes (see also figure 1(b)). Besides the stabilizing effect of the type-II ELM conditions at increased triangularity and q_{95}, the analysis shows that the most unstable mode has a narrower radial extension and becomes more localized to the edge [104].

While the smaller amplitude of type-II ELMs is beneficial, this regime has not yet been obtained at low collisionality. However, if the collisionality at the separatrix is the decisive parameter rather than the pedestal collisionality, the type-II ELMy regime could become a potential candidate for ITER. Type-II ELMs were recently observed in the alternative ITER baseline scenario with $q_{95} = 3.6$ at AUG and were sustained for several seconds [107]. Again, the importance of moving the plasma close to a double-null shape was highlighted in these experiments, further supporting that the plasma shape is key to obtaining small ELMs [102].

3.2. Grassy ELMs

The grassy ELM regime was found on JT-60U [28] in high β_{pol} (>1.6) plasmas with increased triangularity ($\delta > 0.45$) and high edge safety factor ($q_{95} > 6$), but at low collisionality, close to ITER-relevant values. By increasing the triangularity to $\delta > 0.6$ the grassy ELM regime was also sustained at lower q_{95} values, $q_{95} \sim 4$ [108]. Similar to type-II ELMs, grassy ELMs have a very high frequency, ranging from 800-1500 Hz, and small amplitude ($\Delta \mathrm{W_{ELM}/W_{ped}} < 1\%$). Experiments at

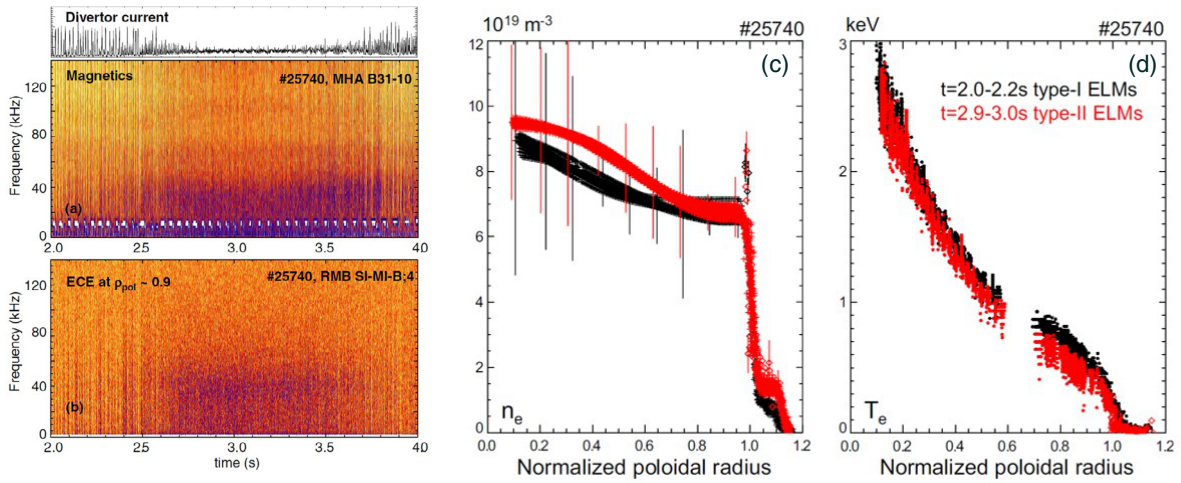

Figure 10. Type-II ELMs at AUG: (*a*) Magnetics spectrogram and divertor current as ELM indicator in the upper panel, (*b*) spectrogram of an ECE channel at the edge showing the onset of a broadband fluctuation as type-II ELMs appear. (*c*) Electron density and (*d*) temperature profile comparing type-I and type-II ELMs. Reproduced from [44]. © IOP Publishing Ltd. All rights reserved.

JT-60U showed that high values of β_{pol} facilitated the access to grassy ELMs, most likely due to the stabilizing effect caused by a strong Shafranov-shift [109, 110]. High β_{pol} plasmas feature two gradient regions, an edge transport barrier and an internal transport barrier in n_e, T_e and T_i located around mid-radius [28]. The importance of β_{pol} for obtaining grassy ELMs was also highlighted in JET experiments [93]. Increasing β_{pol}, achieved by decreasing the plasma current, caused a change in the ELM behaviour and large type-I ELMs were replaced by small-amplitude, high-frequency ELMs.

For grassy ELMs, the pedestal profiles showed a small reduction (less than 20%) in the temperature and density compared to type-I ELMs [28, 111]. No significant magnetic signature was visible. The stability analysis showed that the radial extension of the most unstable mode became narrower compared to type-I ELMs [108] and that the stability boundary is dominated by high-n ballooning modes [112]. The toroidal rotation was found to affect the behaviour of the ELMs and a counter-current rotation facilitated access to the grassy ELM regime [108]. A rotation scan experiment exchanging co- and counter-current beams was performed on JT-60U, demonstrating that with increased rotation in the counter-current direction, with otherwise similar parameters, the type-I ELMs disappeared and were replaced by smaller, grassy ELMs (see figure 11). The impact of rotation and the ion diamagnetic drift effect [113] on the pedestal stability was studied with the MINERVA-DI code [114]. The stabilizing effect of the ion diamagnetic drift pushes the stability boundary away from the operational point, while rotation tends to bring the boundary back, thus competing with the ion diamagnetic drift effect [114]. This further supports that rotation can play a significant role for the pedestal stability.

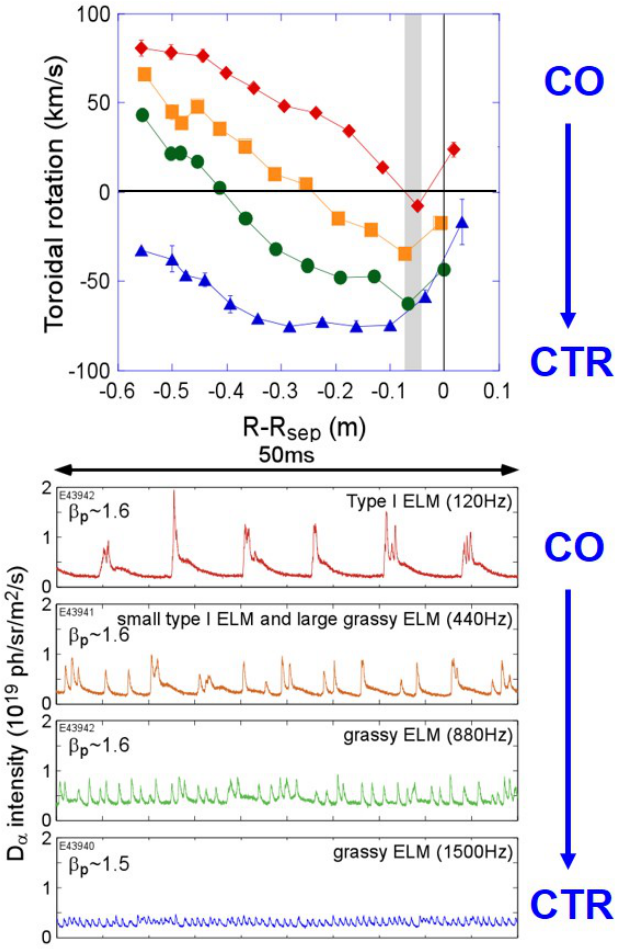

Figure 11. Grassy ELMs at JT-60U: Edge toroidal rotation profiles (upper panel) and time traces of the D_α intensity for the different rotation profiles (lower panel). Reproduced courtesy of IAEA. Figure from [108]. Copyright 2005 IAEA.

4. Comparison of operational space

Substantial progress has been made on developing stationary high-confinement ELM-free and small-ELM regimes. In a variety of regimes, including type-II ELMs, grassy ELMs and the wide-pedestal QH-mode, shaping of the plasma was found to be a key parameter to manipulate the edge stability

and increase the boundary towards higher values of the edge pressure gradient and edge current density. In view of ITER, naturally ELM-free and small-ELM regimes appear attractive, however, a complete physics understanding is required for a meaningful assessment and extrapolation to future fusion devices.

Figure 12 shows a figure of merit for the four regimes discussed in this special topic paper. The star chart displays five coordinates that are relevant for ITER [115], i.e. the pedestal collisionality, triangularity, q_{95}, β_{pol} and the pedestal Greenwald fraction, $f_{\mathrm{GW,\ ped}}$. Note that here $1-f_{\mathrm{GW,\ ped}}$ is plotted. The ITER target values [115] are highlighted with the grey diamond: $\nu^{*}_{\mathrm{ped}}=0.1$, $\delta=0.4$, $q_{95}=3$, $\beta_{\mathrm{pol}}=0.6$ [116], $f_{\mathrm{GW,\ ped}}=0.8$ resulting in $1-f_{\mathrm{GW,\ ped}}=0.2$. It should be noted that in present day machines, some parameters cannot be achieved simultaneously. Low collisionality operation typically means operating at low density and low Greenwald fraction, while ITER will operate at low collisionality but high Greenwald fraction. The coloured, shaded areas in figure 12 correspond to the parameter ranges achieved for the various regimes. The I-mode values represent AUG [46, 47] and C-Mod [48] data, the QH-mode data represents the parameter range obtained at DIII-D [81, 117], which also covers the range for the QH-modes achieved on AUG-C [41], JET-C [42, 69] and JT-60U [43]. The values for type-II ELMs correspond to data from AUG [23, 44] and JET [93] and grassy ELMs to data from JT-60U [28, 108]. The I-mode and the QH-mode cover quite a wide area, in particular in collisionality, triangularity, q_{95} and Greenwald fraction. However, steady operation at high normalized density has not been achieved yet for both regimes. For the QH-mode the operational window towards the ITER relevant low $q_{95}=3$ is currently being extended. The grassy ELMs also span a wide region, however, more experiments are needed to obtain the ITER target, especially in terms of q_{95} and the Greenwald fraction. The type-II ELMs are achieved at the ITER Greenwald fraction and triangularity and were recently obtained in the alternative ITER baseline scenario at $q_{95}=3.6$, but have not yet been observed at ITER-relevant pedestal collisionality values. Future experiments on type-II ELMs should include a β_{pol} scan to clarify whether type-II ELMs can be achieved at the ITER target value of β_{pol}. For a meaningful projection towards ITER and future fusion devices, accessibility studies on a multi-machine basis, similar as done in [48], are needed.

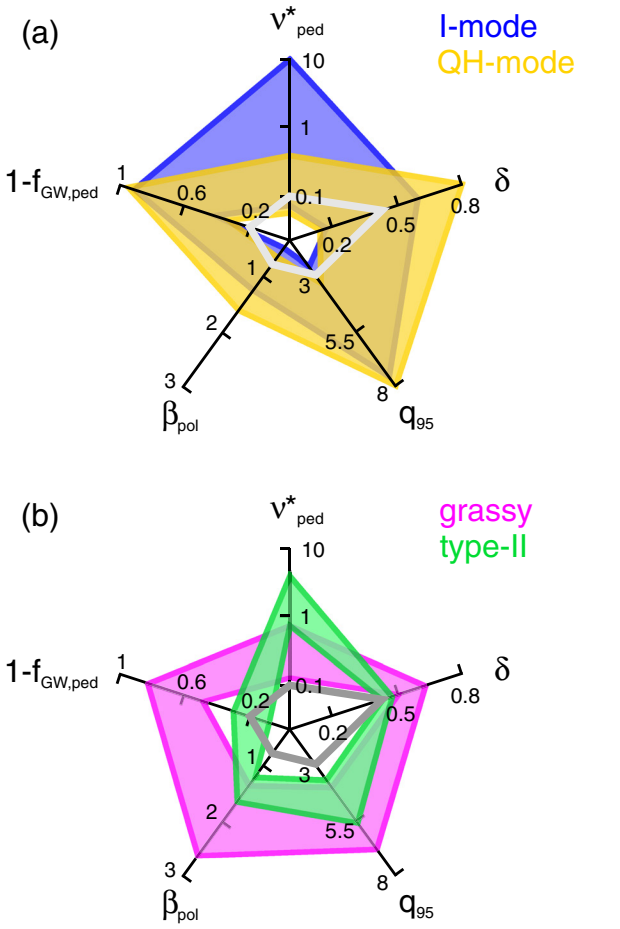

Figure 12. Existence diagram of (*a*) no-ELM regimes and (*b*) small ELMs. The five axes represent the pedestal collisionality ν_{ped}, triangularity δ, q_{95}, β_{pol} and $1-f_{\mathrm{GW,\ ped}}$, $\mathrm{f_{GW,\ ped}}$ being the Greenwald pedestal fraction. The grey diamond represents the ITER target [115].

5. Discussion and conclusions

On the route towards achieving fusion in a magnetic confinement device, ELMs constitute one of the biggest obstacles to steady-state operation. During the last decade, extensive effort has been put into the development of steady quiescent, ELM-free or ELM mitigated regimes. Currently, the two leading strategies for ITER are ELM suppression with externally applied magnetic perturbation coils [25] and ELM-pacing with pellets [35]. The reader is referred to [30] for recent reviews on active ELM control techniques. ELM-free and small-ELM regimes have recently regained attention as alternative scenarios as they can be accessed 'naturally' by e.g. changing the plasma triangularity, local magnetic shear or $\mathbf{E}\times\mathbf{B}$ shear. Naturally occurring ELM-free and small-ELM regimes would be attractive solutions as their ELM energy loss is sufficiently small to obtain minimal transient heat and particle loads combined with sufficient ELM impurity exhaust.

While the different ELM-free and small-ELM regimes reviewed in this work all have different characteristic signatures, one commonality becomes clear: a mechanism is activated which changes the transport and the structure of the pedestal in such a way that it becomes stable against peeling-ballooning modes and thus, no type-I ELM can occur. However, certain boundary conditions have to be introduced in order to open a window for these mechanisms to be activated and to cause enough transport to significantly change the pedestal structure. One of these boundary conditions is high triangularity, which is shown to be important for accessing type-II ELMs, grassy ELMs and the wide-pedestal QH-mode. Higher triangularity shifts the peeling-ballooning stability boundary towards higher pressure gradients and edge currents, thereby opening a larger operational space for local ballooning modes close to the separatrix. A similar boundary condition might be ascribed to rotation (high $\mathbf{E}\times\mathbf{B}$ rotational

shear for the QH-mode, counter-current rotation for grassy ELMs) and to the operation in the unfavourable ∇B drift configuration (I-mode). If in this additionally gained operational space a mechanism is activated which changes the transport in the gradient region, the pedestal structure is also changed. For the cases reviewed here, a microscopic or macroscopic mode develops: the WCM, GAM and intermittent density fluctuations [65] for the I-mode, EHO or broadband MHD [71] for the QH-mode and local ballooning modes at the separatrix for type-II ELMs [105]. Grassy ELMs could be of similar nature. They are observed at low collisionality, high triangularity, high q_{95}, high β_{pol} and exhibit small changes in the pedestal profiles compared to type-I ELMs [28]. In previous work also other modes were found, such as the 'Bursty Chirping Mode' in discharges with lithium injection [118] or the 'Quasi-Coherent' Mode in the EDA H-mode [22, 119], as well as other mechanisms that modify the pedestal structure (in particular the density profile), such as lithium wall conditioning [120] or nitrogen seeding [18, 121]. They all have in common that the pedestal pressure gradient is modified and shifted away from the separatrix, thus improving the pedestal stability towards type-I ELMs [17, 18].

The prospects of these regimes are very promising. While the access conditions for achieving no-ELM and small-ELM regimes are known, a detailed physics understanding is not yet available. The I-mode exhibits properties that are envisaged for future fusion devices, however, so far it has only been obtained robustly in the unfavourable ion ∇B configuration which has a higher L-H power threshold compared to the favourable configuration. The compatibility with the design of future fusion reactors has to be assessed. Experiments at AUG dedicated to increasing the Greenwald fraction of the I-mode and achieving higher β_N values are currently ongoing [67]. The operational window of the QH-mode was extended towards ITER-relevant conditions including high Greenwald fraction and low/zero net torque. However, to date a steady-state QH-mode has not been observed in a metal machine. Part of the EUROfusion MST1 campaign [102] is focussing on developing natural ELM-free and small ELM scenarios, including the QH-mode, at AUG with a tungsten wall, TCV and MAST-U in order to contribute to the physics understanding and to assess the compatibility with a metal wall. A reversed B_t/I_p campaign on AUG is scheduled later in 2018 and foresees the development of the QH-mode and I-mode scenarios in reversed B_t/I_p. The required condition to enter the small ELM regimes in terms of plasma shape has to be assessed since ITER does not foresee a shape close to double-null. It is currently not clear whether the pedestal collisionality or the collisionality at the separatrix is the more important parameter for future machines. In the latter case, type-II ELMs could become a potential candidate. For all regimes more work at ITER and reactor relevant conditions, including low torque input, operation with a partially or even fully detached divertor and pellet fuelling, amongst others, are required. To date, a detached divertor and low collisionality operation are not yet compatible. Understanding the underlying physics mechanism at these conditions is important for extrapolation to future devices.

In summary, substantial progress in understanding and extending the access and sustainment of natural ELM-free and small-ELM regimes has been obtained in the past years. The various regimes reviewed in this work have in common that they exhibit a characteristic mode (or mode coupling) which increases transport in the pedestal region. All these modes are of different nature and it is not yet clear whether they can be obtained in an ITER pedestal and whether they will induce enough transport to keep the pedestal below the peeling-ballooning stability boundary for type-I ELMs. The most important next step is to compare the experimental findings with non-linear MHD and gyrokinetic modelling in order to obtain a detailed understanding of the underlying physics mechanisms that set energy and particle transport in the various regimes. The validation of modelling against experiment is required for a complete physics basis and for improving the predictive capability towards ITER.

Acknowledgments

The author would like to thank C. Angioni, K. H. Burrell, X. Chen, M. G. Dunne, A. Garofalo, T. Happel, M. Hölzl, A. E. Hubbard, Y. Kamada, A. Loarte, F. Liu, R. Maingi, P. Manz, A. Merle, H. Meyer, C. Paz-Soldan, F. Ryter, M. Siccinio, E. Solano, W. Suttrop, H. Urano, T. M. Wilks, E. Wolfrum, H. Zohm and the ITPA Pedestal and Edge Physics Group for fruitful discussions and valuable input.

This work has been partially carried out within the framework of the EUROfusion Consortium and has partially received funding from the Euratom research and training programme 2014-2018 under grant agreement No. 633053. The views and opinions expressed herein do not necessarily reflect those of the European Commission.

The support from the H2020 Marie-Skłodowska Curie programme (Grant No. 708257) and the Spanish Ministry of Economy and Competitiveness (Grant No. FJCI-201422139) is gratefully acknowledged.

ORCID iDs

E. Viezzer https://orcid.org/0000-0001-6419-6848

References

[1] Campbell D.J. and ITER Collaborators 2012 Challenges in burning plasma physics: the ITER research plan, ITR/P1-18 *Proc. 24th Int. Atomic Energy Agency Conf. on Fusion Energy (San Diego, 8–13 October 2012)* [ITR/P1-18] (www-naweb.iaea.org/napc/physics/FEC/FEC2012/papers/620_ITRP118.pdf)
[2] Wagner F. *et al* 1982 *Phys. Rev. Lett.* **49** 1408
[3] Zohm H. 1996 *Plasma Phys. Control. Fusion* **38** 105
[4] Loarte A. *et al* 2006 *Nat. Phys.* **2** 369
[5] Wilson H. *et al* 2006 *Plasma Phys. Control. Fusion* **48** A71
[6] Wilson H. *et al* 2008 *Fusion Sci. Technol.* **53** 161
[7] Leonard A.W. *et al* 2014 *Phys. Plasmas* **21** 090501
[8] Gohil P. *et al* 1988 *Phys. Rev. Lett.* **61** 1603

[9] Huysmans G.T.A. *et al* 1995 *22nd EPS Conf. on Plasma Physics, Europhysics Conf. Abstracts Vol. 19C (Bournemouth, UK, 3–7 July 1995)* (http://iopscience.iop.org/issue/0741-3335/37/11A)
[10] Connor J.W. *et al* 1998 *Phys. Plasmas* **5** 2687
[11] Snyder P.B. *et al* 2002 *Phys. Plasmas* **9** 2037
[12] Eich T. *et al* 2011 *Phys. Rev. Lett.* **107** 215001
[13] Loarte A. *et al* 2003 *Plasma Phys. Control. Fusion* **45** 1549
[14] Loarte A. *et al* 2014 *Nucl. Fusion* **54** 033007
[15] Dickinson D. *et al* 2014 *Phys. Plasmas* **21** 010702
[16] Bokshi A. *et al* 2016 *Plasma Phys. Control. Fusion* **58** 075011
[17] Wolfrum E. *et al* 2017 *Nucl. Mater. Energy* **12** 18
[18] Dunne M.G. *et al* 2017 *Plasma Phys. Control. Fusion* **59** 025010
[19] Zohm H. 2015 *Magnetohydrodynamic Stability of Tokamaks* (New York: Wiley)
[20] Burrell K.H. *et al* 2001 *Phys. Plasmas* **8** 2153
[21] Whyte D. *et al* 2010 *Nucl. Fusion* **50** 105005
[22] Greenwald M. *et al* 1997 *Nucl. Fusion* **37** 793
[23] Stober J. *et al* 2001 *Nucl. Fusion* **41** 1123
[24] Oyama N. *et al* 2006 *Plasma Phys. Control. Fusion* **48** A171
[25] Evans T.E. *et al* 2006 *Nat. Phys.* **2** 419
[26] Suttrop W. *et al* 2011 *Phys. Rev. Lett.* **106**
[27] Jeon Y.M. *et al* 2012 *Phys. Rev. Lett.* **109** 035004
[28] Kamada Y. *et al* 2000 *Plasma Phys. Control. Fusion* **42** A247
[29] Liang Y. *et al* 2011 *Fusion Sci. Technol.* **59** 586
[30] Maingi R. *et al* 2014 *Nucl. Fusion* **54** 114016
[31] Evans T.E. *et al* 2004 *Phys. Rev. Lett.* **92** 235003
[32] Suttrop W. *et al* 2017 *Plasma Phys. Control. Fusion* **59** 014050
[33] Lang P.T. *et al* 2004 *Nucl. Fusion* **44** 665
[34] Baylor L.R. *et al* 2009 *Nucl. Fusion* **49** 085013
[35] Lang P.T. *et al* 2013 *Nucl. Fusion* **53** 043004
[36] Degeling A.W. *et al* 2003 *Plasma Phys. Control. Fusion* **45** 1637
[37] de la Luna E. *et al* 2016 *Nucl. Fusion* **56** 026001
[38] Kim J. *et al* 2012 *Nucl. Fusion* **52** 114011
[39] Xiao W.W. *et al* 2012 *Nucl. Fusion* **52** 114027
[40] Ryter F. *et al* 1998 *Plasma Phys. Control. Fusion* **40** 725
[41] Suttrop W. *et al* 2003 *Plasma Phys. Control. Fusion* **45** 1399
[42] Solano E.R. *et al* 2010 *Phys. Rev. Lett.* **104** 185003
[43] Sakamoto Y. *et al* 2004 *Plasma Phys. Control. Fusion* **46** A299
[44] Wolfrum E. *et al* 2011 *Plasma Phys. Control. Fusion* **53** 085026
[45] ITER Physics Expert Group on Confinement and Transport *et al* 1999 *Nucl. Fusion* **39** 2175
[46] Happel T. *et al* 2017 *Plasma Phys. Control. Fusion* **59** 014004
[47] Ryter F. *et al* 2017 *Nucl. Fusion* **57** 016004
[48] Hubbard A.E. *et al* 2016 *Nucl. Fusion* **56** 086003
[49] Hubbard A.E. *et al* 2017 *Nucl. Fusion* **57** 126039
[50] Hubbard A.E. *et al* 2011 *Phys. Plasmas* **18** 056115
[51] White A.E. *et al* 2011 *Nucl. Fusion* **51** 113005
[52] Cziegler I. *et al* 2013 *Phys. Plasmas* **20** 055904
[53] Manz P. *et al* 2015 *Nucl. Fusion* **55** 083004
[54] Marinoni A. *et al* 2015 *Nucl. Fusion* **55** 093019
[55] Hubbard A.E. *et al* 2012 *Nucl. Fusion* **52** 114009
[56] Ryter F. *et al* 2014 *Nucl. Fusion* **54** 083003
[57] Stroth U. *et al* 2011 *Plasma Phys. Control. Fusion* **53** 024006
[58] McDermott R.M. *et al* 2009 *Phys. Plasmas* **16** 056103
[59] Viezzer E. *et al* 2014 *Nucl. Fusion* **54** 012003
[60] Cavedon M. *et al* 2017 *Nucl. Fusion* **57** 014002
[61] Martin Y.R. *et al* 2008 *J. Phys.: Conf. Ser.* **123** 012033
[62] Theiler C. *et al* 2014 *Nucl. Fusion* **54** 083017
[63] Sauter P. *et al* 2012 *Nucl. Fusion* **52** 012001
[64] Cavedon M. *et al* 2018 in preparation
[65] Happel T. *et al* 2016 *Nucl. Fusion* **56** 064004
[66] Manz P. *et al* 2017 *Nucl. Fusion* **57** 086022
[67] Happel T. *et al* 2018 *23rd Int. Conf. on Plasma Surface Interactions in Controlled Fusion Devices (Princeton, 17–22 June 2018)* (https://psi2018.princeton.edu/)
[68] Merle A. *et al* 2017 *59th Annual Meeting of the APS Division of Plasma Physics (Milwaukee, 23–27 October 2017)* UP11.00072 (https://meetings.aps.org/Meeting/DPP17/Session/UP11.71)
[69] Suttrop W. *et al* 2005 *Nucl. Fusion* **45** 721
[70] Burrell K.H. *et al* 2002 *Plasma Phys. Control. Fusion* **44** A253
[71] Burrell K.H. *et al* 2016 *Phys. Plasmas* **23** 056103
[72] Burrell K.H. *et al* 2009 *Nucl. Fusion* **55** 085042
[73] Huysmans G.T.A. *et al* 2007 *Nucl. Fusion* **47** 659
[74] Sovinec C.R. *et al* 2004 *J. Comput. Phys.* **195** 355
[75] Liu F. *et al* 2015 *Nucl. Fusion* **55** 113002
[76] Liu F. *et al* 2016 *Preprint: 2016 IAEA FEC Conf. (Kyoto, Japan, 17–22 October 2016)* (https://conferences.iaea.org/indico/event/98/session/18/contribution/648)
[77] King J. *et al* 2017 *Nucl. Fusion* **57** 022002
[78] King J. *et al* 2017 *Phys. Plasmas* **24** 055902
[79] Krebs I. *et al* 2013 *Phys. Plasmas* **20** 082506
[80] Liu F. *et al* 2018 *Plasma Phys. Control. Fusion* **60** 014039
[81] Solomon W.M. *et al* 2015 *Nucl. Fusion* **55** 073031
[82] Garofalo A. *et al* 2015 *Phys. Plasmas* **22** 056116
[83] Burrell K.H. *et al* 2009 *Phys. Rev. Lett.* **102** 155003
[84] Garofalo A. *et al* 2011 *Nucl. Fusion* **51** 083018
[85] Chen X. *et al* 2016 *Nucl. Fusion* **56** 076011
[86] Chen X. *et al* 2017 *Nucl. Fusion* **57** 086008
[87] Wilks T.M. *et al* 2018 *Nucl. Fusion* **58** 112002
[88] Snyder P.B. *et al* 2007 *Nucl. Fusion* **47** 961
[89] Chen X. *et al* 2017 *Nucl. Fusion* **57** 022007
[90] Burrell K.H. *et al* 2017 *59th Annual Meeting of the APS Division of Plasma Physics, PO4.011 (Milwaukee, 23–27 October 2017)*
[91] Chen X. *et al* 2018 *Nucl. Fusion* submitted
[92] Ozeki T. *et al* 1990 *Nucl. Fusion* **30** 1425
[93] Saibene G. *et al* 2005 *Nucl. Fusion* **45** 297
[94] Stober J. *et al* 2005 *Nucl. Fusion* **45** 1213
[95] Saarelma S. *et al* 2009 *Plasma Phys. Control. Fusion* **51** 035001
[96] Kamiya K. *et al* 2003 *Nucl. Fusion* **43** 1214
[97] Maingi R. *et al* 2005 *Nucl. Fusion* **45** 1066
[98] Xu G.S. *et al* 2017 *44th EPS Conf. on Plasma Physics (Belfast, UK, 26–30 June 2017)* (http://ocs.ciemat.es/EPS2017PAP/html/)
[99] Kamiya K. *et al* 2007 *Plasma Phys. Control. Fusion* **49** S43
[100] Wolfrum E. *et al* 2015 *42nd EPS Conference on Plasma Physics (Lisbon, Portugal, 22–26 June 2015)* (http://ocs.ciemat.es/EPS2015PAP/pdf/P1.115.pdf)
[101] Chapman I.T. *et al* 2016 *Plasma Phys. Control. Fusion* **58** 014017
[102] Meyer H. *et al* 2017 *Nucl. Fusion* **57** 102014
[103] Doyle E.J. *et al* 1991 *Phys. Fluids* B **3** 2300
[104] Saarelma S. *et al* 2003 *Nucl. Fusion* **43** 262
[105] Harrer G.F. *et al* 2018 *Nucl. Fusion* submitted
[106] Kirk A. *et al* 2011 *Plasma Phys. Control. Fusion* **53** 095008
[107] Schweinzer J. *et al* 2016 *Nucl. Fusion* **56** 106007
[108] Oyama N. *et al* 2005 *Nucl. Fusion* **45** 871
[109] Kamada Y. *et al* 2002 *Plasma Phys. Control. Fusion* **44**
[110] Saarelma S. *et al* 2004 *Plasma Phys. Control. Fusion* **46** 1259
[111] Kojima A. *et al* 2009 *Nucl. Fusion* **49** 115008
[112] Aiba N. *et al* 2012 *Nucl. Fusion* **52** 114002
[113] Tang W.M. *et al* 1980 *Nucl. Fusion* **20** 1439
[114] Aiba N. *et al* 2017 *Nucl. Fusion* **57** 022011
[115] ITER Physics Basis 2007 *Nucl. Fusion* **47(6)**
[116] Green B.J. *et al* 2003 *Plasma Phys. Control. Fusion* **45** 687
[117] Burrell K.H. *et al* 2005 *Phys. Plasmas* **12** 056121
[118] Osborne T.H. *et al* 2015 *Nucl. Fusion* **55** 063018
[119] LaBombard B. *et al* 2014 *Phys. Plasmas* **21** 056108
[120] Maingi R. *et al* 2009 *Phys. Rev. Lett.* **103** 075001
[121] Dunne M.G. *et al* 2017 *Nucl. Fusion* **57** 025002